SUPPLEMENTAL MATERIAL

A non-invasive sub-surface electrical probe to encapsulated layers in van der Waals heterostructures

Mrityunjay Pandey,[1,*] Radhika Soni,[2] Avi Mathur,[2] Akash Singh,[3]
Abhishek Kumar Singh,[3] Srinivasan Raghavan,[1] and U. Chandni[2,†]

[1] *Centre for Nano Science and Engineering, Indian Institute of Science, Bangalore 560012, India*
[2] *Department of Instrumentation and Applied Physics, Indian Institute of Science, Bangalore 560012, India*
[3] *Materials Research Centre, Indian Institute of Science, Bangalore 560012, India*

A. MODELING OF TIP-SAMPLE CAPACITIVE COUPLING

The capacitive coupling between an AFM tip and a metal layer can be modelled by considering the tip to comprise of apex, cone and cantilever regions. The net capacitance can be modelled using a parallel combination of plate capacitors. In the model presented here we have ignored the cantilever component as its contribution to the EFM phase is minimal [1]. Below, we have used the analytical expressions for the capacitances of apex and cone to understand the effect of the capacitive coupling term (second derivative $\frac{d^2C}{dz^2}$) on the EFM phase.

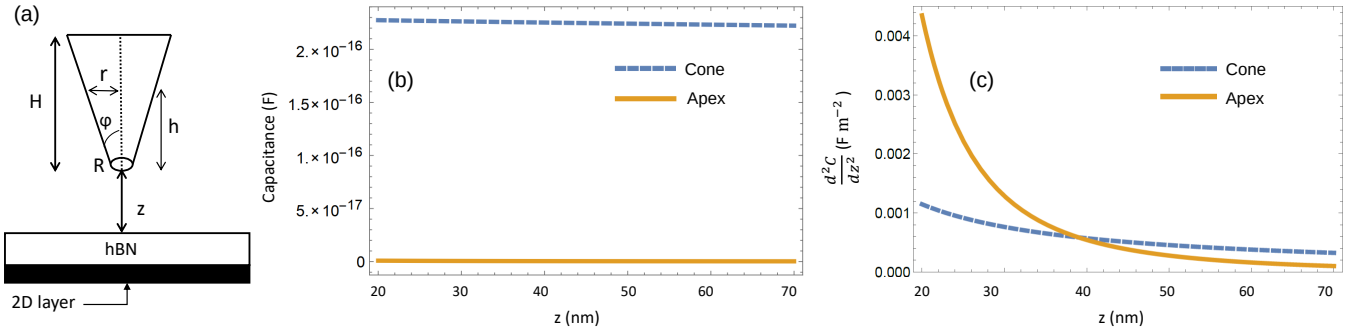

Fig. S1: (a) Schematic showing the AFM tip and a typical heterostructure geometry. Analytical calculations for the (b) capacitance and (c) second derivative of capcitance or the capacitive coupling term, for a metal probe metal surface system, plotted as a function of tip-sample separation z, showing contributions from the apex and cone regions of the AFM tip.

Consider the AFM tip to have a geometry as shown in Fig.S1(a) with a tip height H and the height between tip and the heterostructure to be z (includes the lift height and amplitude set points). For the Pt-Ir tip used in this work, the apex radius is $R = 25$ nm, height $H = 10\,\mu$m, angle $\phi = 22.5^o$ and $z \sim 20 - 30$ nm. The capacitance between tip and a flat sample surface encapsulated with a top layer of hBN (~ 30 nm) can be expressed as:

$$C_{\text{tip}} \approx C_{\text{apex}} + C_{\text{cone}} \tag{1}$$

$$C_{\text{apex}} = \frac{\varepsilon_0 \pi R^2}{t_{\text{hBN}} + z} \tag{2}$$

where $t_{\text{hBN}} = \frac{\text{thickness of hBN}}{\text{dielectric constant of hBN}}$ is the effective thickness of the top hBN layer. Dielectric constant of hBN is taken to be 4.

$$C_{\text{cone}} = \int_0^H \frac{2\pi\epsilon_0 h \tan\phi}{z + t_{\text{hBN}} + h} dh \tag{3}$$

where $r = h \tan\phi$ (See Fig.S1(a))

$$C_{\text{cone}} = 2\pi\epsilon_0(z + t_{\text{hBN}}) \tan\phi \left[\frac{H}{z + t_{\text{hBN}}} - \ln\left(\frac{H + z + t_{\text{hBN}}}{z + t_{\text{hBN}}} \right) \right] \tag{4}$$

This gives the effective capacitive coupling term for the system to be:

$$\frac{d^2C_{\text{tip}}}{dz^2} \approx \frac{d^2C_{\text{cone}}}{dz^2} + \frac{d^2C_{\text{apex}}}{dz^2} \tag{5}$$

For the Pt-Ir tip used in this work, the capacitance C_{tip} and the capacitive coupling term as a function of z are shown in Fig.S1(b) and (c) respectively. It is evident that the capacitive coupling term is dominated by the apex region for $z \leq 30$ nm.

This model for capacitance works fairly well for samples where the *dc* voltage is applied directly between the sample and the tip (Fig.S2(a)), and gives the electrostatic phase as $\tan(\Delta\phi) = \frac{Q}{k}\frac{dF}{dz} = \frac{-Q}{2k}\frac{d^2C_{\text{tip}}}{dz^2}(V_{dc} - V_s)^2$, where Q and k are the quality factor and the spring constant of the cantilever, respectively. V_s is the contact potential difference; $V_s = \Phi_s - \Phi_t$, where Φ_s is the work function of the sample and Φ_t is the work function of the AFM probe.

In our samples, the *dc* voltage is applied between the tip and the doped Si back gate with a floating encapsulated 2D layer (Fig.S2(b)). In the following, we estimate the capacitive coupling and voltage drops in such a heterostructure geometry by considering two capacitors in series, defined as C_1 and C_2 (Fig.S2(c)). It is to be noted that in this geometry, while the tip is of radius $R \sim 25$ nm, the lateral dimensions of the 2D layer are of the order of tens of microns. This would lead to significant fringing effects. For simplicity, we assume parallel plate capacitors, which provide reasonable qualitative estimates. C_1 is the capacitance between the AFM tip and the 2D layer, with air and top hBN being the two different dielectric materials between the capacitor plates. Capacitance $C_1 = C_{\text{tip}}$ can be written in a simplified form considering an effective area A_1

$$C_1 \approx \frac{A_1\varepsilon_0}{z + t_{\text{hBN}}} \tag{6}$$

where t_{hBN} is the effective thickness of top hBN normalised by the dielectric constant.

Further, the capacitance between graphene and silicon backgate C_2, with the bottom hBN and silicon dioxide (SiO_2) being the two different dielectric layers, can be written as:

$$C_2 = \frac{A_2\varepsilon_0}{d_{\text{hBN}} + t_{\text{SiO}_2}} \tag{7}$$

where A_2 is the area of the encapsulated 2D layer, d_{hBN} is the effective thickness of bottom hBN and t_{SiO_2} is the effective thickness of SiO_2.

The series combination of these two capacitors gives the total capacitance to be

$$\frac{1}{C_{\text{tot}}} = \frac{1}{C_1} + \frac{1}{C_2} \tag{8}$$

If V_{dc} is the *dc* voltage applied across the tip and the Si back gate, the voltage drops V_1 and V_2 across C_1 and C_2 respectively are given by

$$V_1 = \frac{C_{\text{tot}}V_{dc}}{C_1} \text{ and } V_2 = \frac{C_{\text{tot}}V_{dc}}{C_2} \tag{9}$$

Here, $A_2 >> A_1$, which gives $V_1 \approx V_{dc}$, with most of the voltage applied dropping across the tip - 2D layer capacitor.

Thus, assuming that the major contribution to the EFM phase comes from C_1, the electrostatic force can be written as

$$F = -\frac{1}{2}\frac{dC_1}{dz}[V_{dc} - V_s]^2 \tag{10}$$

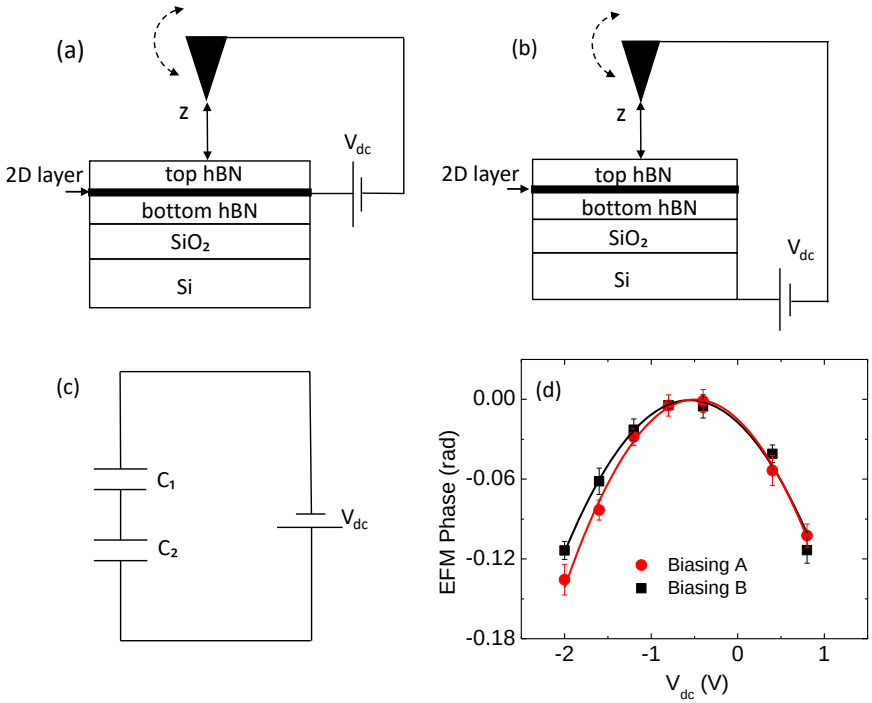

Fig. S2: Two different biasing configurations used to better understand the EFM model. In configuration A shown in (a), the 2D layer is directly biased, where as in configuration B shown in (b), the biasing is done using the doped Si back gate with the 2D layer floating. (c) Biasing configuration B can be modelled using two capacitors C_1 and C_2. (d) Experimentally measured EFM phase plots for the two different configurations.

The electrostatic phase is thus defined as

$$\tan(\Delta\phi) = \frac{Q}{k}\frac{dF}{dz} = \frac{-Q}{2k}\frac{d^2C_1}{dz^2}\left(V_{dc} - V_s\right)^2 \tag{11}$$

This gives a characteristic parabolic dependence of the EFM phase on the tip voltage. In the experiments, the capacitance $C_1 = C_{\rm tip}$ will have contributions from all three regions, namely apex, cone and cantilever. Even in this case, it is reasonable to assume that the capacitance $C_{\rm tot} \approx C_1$, as $C_2 >> C_1$, due to the large lateral spread of the 2D layer. We have further verified this experimentally using two different biasing configurations as detailed below.

B. VERIFICATION OF THE EFM MODEL

In order to verify the model presented above, two different biasing configurations were tested for an encapsulated graphene heterostructure device (hBN/graphene/hBN). In biasing configuration A, a Cr/Au electrode on graphene was used for biasing the encapsulated graphene directly. In biasing configuration B, V_{dc} was applied between the tip and the doped Si back gate. The EFM phase parabolas for the two configurations are shown in Fig. S2(d). It is clear that the EFM parabolas are very similar for both the configurations verifying our model and the conclusion that the biasing voltage V_{dc} drops across the top capacitance C_1. Fits to equation (11) give $V_s = -0.49$ V and -0.55 V for biasing configurations A and B respectively. The capacitive coupling was found to be $C_0 = 0.062$ V^{-2} and 0.054 V^{-2} respectively. The quantitative difference between the analysis on the two configurations was found to be of the order of 10%. In the bias configuration B, assuming that the voltage drop across the top capacitor C_1 is a fraction of $V_{\rm dc}$, $V_1 = V_{\rm dc}/x$, with $x > 1$, the EFM phase can be written as:

$$\tan(\Delta\phi) = \frac{Q}{k}\frac{dF}{dz} = \frac{-Q}{2k}\frac{d^2C_1}{dz^2}\frac{1}{x^2}\left(V_{dc} - xV_s\right)^2 \tag{12}$$

This indicates that the floating configuration B gives a shifted parabola with respect to the configuration A, with a lower curvature, as can be readily seen in Fig. S2(d). A fit to this equation, gives $x = 1.07$, indicating that most of the voltage V_{dc} indeed drops across the capacitor C_1. We have therefore used equation (11) to estimate the workfunctions and capacitive coupling in this work, consistent with previous reports on samples with floating geometries [2, 3].

C. EFM ON TMDC HETEROSTRUCTURES

TMDC heterostructures comprising encapsulated layers of MoS_2 and WSe_2 were studied using the EFM technqiue. Earlier studies of EFM on TMDC flakes on SiO_2/Si wafers had probed the incomplete screening of the charge traps in the SiO_2 layer [4]. In Fig.S3, we show the EFM phase plots for few layer encapsulated MoS_2 and WSe_2 flakes. In Fig.S3(b), we observe that the V_s values obtained for the encapsulated few layer MoS_2 flake is very different from the value obtained for the bulk MoS_2 flake on SiO_2 substrate. This indicates that the quantitative estimates of the V_s values strongly depend on thickness, substrates, charge environment and adsorbed layers.

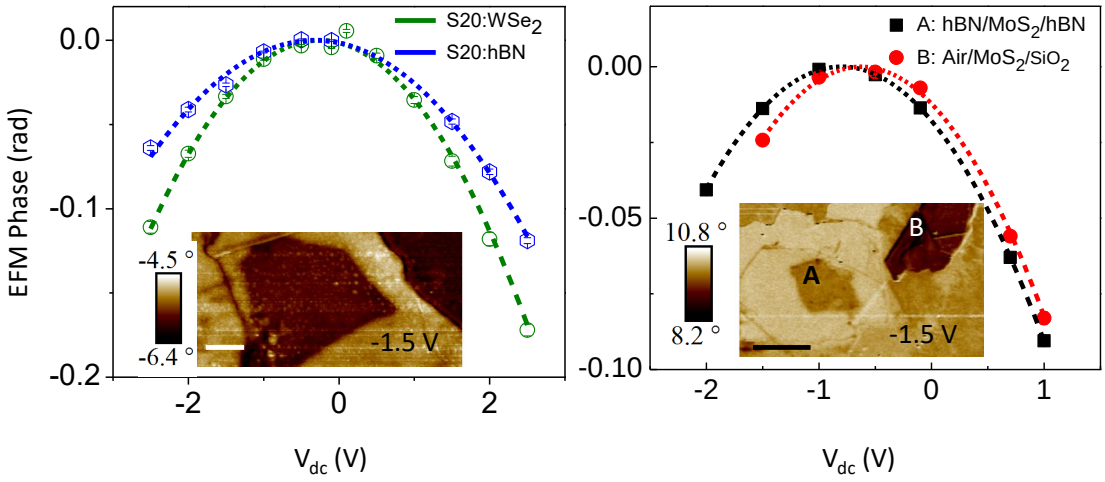

Fig. S3: (a) EFM phase plot for an encapsulated FL-WSe_2 stack S20, showing clear distinction between the constituent hBN and WSe_2 layers. Inset shows the EFM phase image at -1.5 V. The dashed lines indicate fit to equation (11), giving the surface potential $V_s = -0.26$ V, and the capacitive coupling $C_0 = 0.022$ V^{-2} for the encapsulated WSe_2. Scale bar is 1 μm. (b) EFM phase plot for an encapsulated FL-MoS_2 stack S21 marked as region A and a bulk MoS_2 flake on SiO_2 marked as region B. The dashed lines indicate fit to equation 11, giving the surface potential $V_s = -0.79$ V, and the capacitive coupling $C_0 = 0.028$ V^{-2} for region A and $V_s = -0.62$ V, and $C_0 = 0.031$ V^{-2} for region B, respectively. Scale bar is 4 μm.

We also report the EFM phase shifts obtained for three stacks consisting of heterostructures of MoS_2 and WSe_2 sandwiched between hBN layers. While stacks S37 and S18 had a device architecture from top to bottom given by hBN/MoS_2/WSe_2/hBN/SiO_2, in stack 35, the architecture was hBN/WSe_2/MoS_2/hBN/SiO_2. We observed that the quantitative estimates of V_s showed slight variations (up to 0.4 V) across devices, possibly due to adsorbed molecules, water vapor or the effects of extraneous charges. Nevertheless, certain features stand out and remain consistent across devices. Fig.S4 shows the EFM phase plots for the three stacks. It was observed that the capacitive coupling was found to be the nearly the same across the different regions in the stacks. It is noted that in stack 18, the WSe_2 region showed a marginally lower curvature, possibly due to inhomogeniety in the stack. Remarkably, it was also seen that the EFM parabola for the overlapping heterostructure region (A) lay in between the EFM parabolas for the encapsulated WSe_2 (B) and MoS_2 (C) regions, in all the three samples. We speculate this to be due to charge redistribution in the heterostructure. Furthermore, the V_s values for the overlapped region was found to be closer to the MoS_2 layer in all samples tested, irrespective of the heterostructure ordering. This indicates a difference in dielectric screening between the MoS_2 and WSe_2 layers, and poor screening of the heterostructure region by the WSe_2 layer, as elaborated below.

Sulfur vacancies are one of the most frequently observed point defects in MoS_2 [5], with a defect formation energy

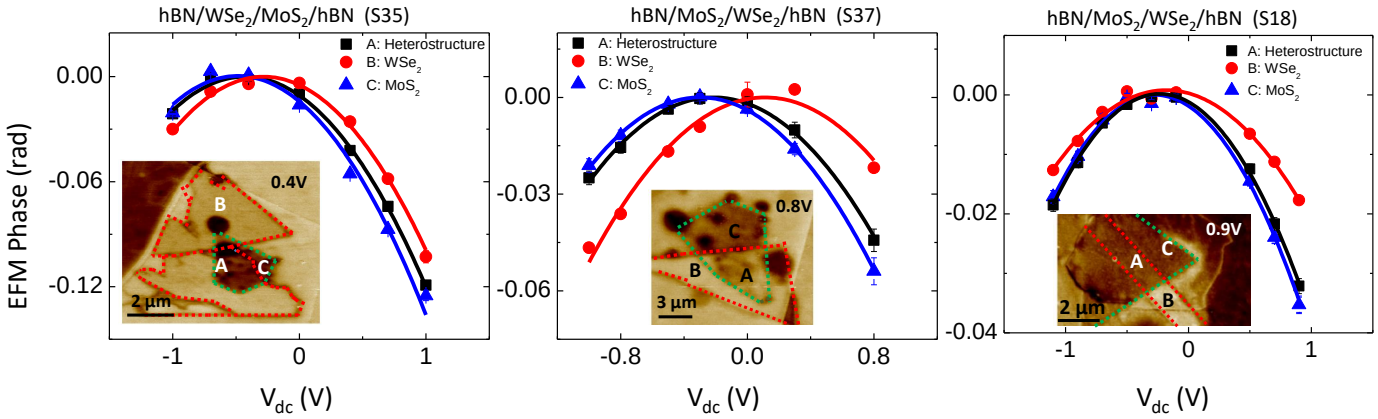

Stack	Lift Height (nm)	Thickness (nm)			V_s (V)			C_0 (V^{-2})		
		MoS_2	WSe_2	hBN	MoS_2	WSe_2	Heterostructure	MoS_2	WSe_2	Heterostructure
S35	20	2.3	2.2	10	-0.48	-0.28	-0.43	0.062	0.060	0.059
S37	20	4.5	6.6	20	-0.29	0.11	-0.21	0.044	0.041	0.042
S18	30	Few layers	Few layers	24	-0.27	-0.18	-0.23	0.025	0.016	0.025

Fig. S5: EFM phase parabolas for the heterostructure region A (black squares), WSe_2 region B (red circles) and MoS_2 region C (blue triangles), for three different stacks (a) stack 37, (b) stack 35 and (c) stack 18. The solid lines are fits to equation (11). Inset shows the EFM phase images for the corresponding stacks showing the three different regions A, B and C. Green and red dashed lines indicate MoS_2 and WSe_2 regions respectively. (d) Table shows the details of the lift height, flake thickness, fit parameters V_s and capacitive coupling C_0, for the different stacks. For stack 18, the flake thicknesses for the few layer MoS_2 and WSe_2 were not measured prior to the creation of the vdW heterostructure.

of ~ 1.3 eV [6], corresponding to $1.0 - 7.8 \times 10^{16}$ cm^{-3} concentration in the bulk limit. A recent study [7] showed that the sulfur vacancies provide electron trap centers near the conduction band, which quench the mobile electron carriers rather than providing free electron carriers. Moreover, these vacancies provide strongly localized charge density around the defect centre. The defect formation energy of selenium vacancies is 3.1 eV in bulk WSe_2, which is higher than formation energy of sulphur vacancies in MoS_2, giving a lower concentration of selenium vacancies (2.87×10^{12} cm^{-3}) [8]. Therefore, the localized defect charge densities of the sulphur vacancies in MoS_2 is much higher than the selenium vacancies in WSe_2. We have calculated the dielectric constants of MoS_2, WSe_2 and the van der Waal heterostructures of MoS_2/WSe_2 using the density functional perturbation theory [9]. In heterostructures of MoS_2/WSe_2, the enhanced charge density due the point defects in the WSe_2 layer will be strongly screened by the MoS_2 layer as the static dielectric environment of MoS_2 ($\epsilon_{xx} = \epsilon_{yy} = 15.3$ for single-layer and $\epsilon_{xx} = \epsilon_{yy} = 16.3$ for bulk) is higher than WSe_2 ($\epsilon_{xx} = \epsilon_{yy} = 13.1$ for single-layer, and $\epsilon_{xx} = \epsilon_{yy} = 14.1$ for bulk). Therefore, the measured EFM phase in the heterostructure region is expected to be shifted towards the MoS_2 layer.

D. SUMMARY OF EFM EXPERIMENTS

Sample	Bottom hBN (nm)	Top hBN (nm)	Lift Height (nm)	C_0 (V^{-2})	V_s (V)
S14: hBN/SLG/hBN	28	13	30	0.031	-0.46
S15: hBN/SLG/SiO_2	33	18	30	0.026	-1.06
S15: hBN/SLG/hBN	33	18	30	0.031	-0.66
S8: hBN/FLG/hBN	27	25	20	0.067	-0.39
S8: Air/FLG/hBN	27	25	20	0.072	-0.23
S11: hBN/FLG/hBN	27	27	30	0.040	-0.45
S11: Air/FLG/hBN	27	27	30	0.050	-0.36
S20: hBN/FL-WSe_2/hBN	24	18	30	0.022	-0.26
S21: hBN/FL-MoS_2/hBN	34	12	30	0.028	-0.79
S39: hBN/4.8nm-WSe_2/hBN	5.7	13	30	0.037	-0.17
S38: hBN/2.2nm-MoS_2/hBN	15	15	20	0.062	-0.61

Table 1: Table summarizing the results obtained for various encapsulated graphene and TMDC heterostructures, indicating top and bottom hBN thicknesses, lift height and fit parameters C_0 and V_s obtained from equation (11). Within a stack the variations in capacitive coupling is expected to be minimal. The major factor responsible for phase variance is the change in the surface potential of the constituent layers.

* mrityunjay@iisc.ac.in
† chandniu@iisc.ac.in

[1] C. H. Lei, A. Das, M. Elliott and J. E. Macdonald, Quantitative electrostatic force microscopy-phase measurements, Nanotechnology **15**, 627 (2004).
[2] S. S. Datta, D. R. Strachan, E. J. Mele, and A. T. Charlie Johnson, Surface Potentials and Layer Charge Distributions in Few-Layer Graphene Films, Nano Lett. **9**, 7 (2009).
[3] Y. Shi, X. Dong, P. Chen, J. Wang and L-J. Li, Effective doping of single-layer graphene from underlying SiO_2 substrates Phys. Rev. B. **79**, 115402 (2009).
[4] A. CastellanosGomez, E. Cappelluti, R. Roldn, N. Agrat, F. Guinea and G. RubioBollinger, ElectricField Screening in Atomically Thin Layers of MoS_2: the Role of Interlayer Coupling, Adv. Mater. **25**, 899 (2012).
[5] W. Zhou, X. Zou, S. Najmaei, Z. Liu, Y. Shi, J. Kong, J. Lou, P. M. Ajayan, B. I. Yakobson,and J-C. Idrobo, Intrinsic Structural Defects in Monolayer Molybdenum Disulfide, Nano Lett **13**, 2615 (2013).
[6] J-Y. Noh, H. Kim, and Y-S. Kim, Stability and electronic structures of native defects in single-layer MoS_2, Phys. Rev. B. **89**, 205417 (2014).
[7] A. Singh and A. K. Singh, Origin of n-type conductivity of monolayer MoS_2, Phys. Rev. B. **99**, 121201 (2019).
[8] D. Han, W. Ming, H. Xu, S. Chen, D. Sun, and M-H. Du, Chemical Trend of Transition-Metal Doping in WSe_2, Phys. Rev. A, **12**, 034038 (2019).
[9] A. Debernardi, and S. Baroni, Third-Order Density-Functional Perturbation Theory: A Practical Implementation with Applications to Anharmonic Couplings in Si, Solid State Commun., **91**, 813 (1994).